AIAA Journal
Vol. 48, No. 8, August 2010

Aerothermodynamics Behind a Blunt Body at Superorbital Speeds

Gisu Park,* Sudhir L. Gai,† and Andrew J. Neely‡
University of New South Wales, Canberra, Australian Capital Territory 2600, Australia

DOI: 10.2514/1.J050251

Results of an experimental, numerical, and analytical study of the hypersonic laminar near-wake flow of a 45° half-angle blunted cone are presented. A superorbital expansion tube facility, which can generate different planetary atmospheric compositions, was used for the experiments. In the present instance, two test gases [air and a mixture of 96%CO_2-4%N_2 (simulating the Martian atmosphere)] were used. Superorbital speeds above 8 km/s were generated at specific enthalpies of 44.5 MJ/kg (air) and 32.9 MJ/kg (96%CO_2-4%N_2). Measurements consisted of surface pressure and heat flux, and both showed good agreement with theoretical and numerical predictions. It was also noted that, based on numerical data, chemical reactions seemed to be stronger in the case of the test gas simulating the Martian atmospheric composition when compared with those of air.

Nomenclature

A = base surface area, m^2
C = Chapman–Rubesin constant ($\rho\mu/\rho_e\mu_e$)
C_f = skin-friction coefficient ($2\tau_w/(\rho_\infty u_\infty^2)$)
c_L = centerline (Fig. 1)
c_p = specific heat at constant pressure, J/(kg · K)
c_v = specific heat at constant volume, J/(kg · K)
D = model diameter, m
D_{12} = diffusion coefficient of a binary gas
F = shear function [Eq. (14)]
H = total specific enthalpy, J/kg ($h + u^2/2$)
h = static enthalpy, J/kg
k = thermal conductivity, W/(m · K)
Le = Lewis number ($\rho D_{12} c_p/k$)
M = Mach number [$u/(\gamma RT)^{1/2}$]
n = bluntness ratio (R_{nose}/R)
Pr = Prandtl number ($\mu c_p/k$)
p = static pressure, Pa
Q = total heat flux, W
q = heat flux, W/m^2 [Eq. (1)]
R = model radius, m
R = specific gas constant, J/(kg · K)
R_{nose} = nose radius, m
R_{shoulder} = shoulder radius, m
Re = Reynolds number ($\rho u D/\mu$)
S = reduced streamwise distance [Eq. (16)]
S_w = parameter S evaluated for body [Eq. (10)]
St = Stanton number [Eq. (2)]
s = distance from the front stagnation point, m (Fig. 1)
T = temperature, K
t = time, s
u = velocity, m/s
u^* = velocity ratio [Eq. (5)]
V = voltage, V
X = mass fraction
x = distance along the free shear layer from flow separation point, m (Fig. 1)
x_b = axial distance from the base, m (Fig. 1)
Y = transformed normal distance [Eq. (15)]
y = distance normal to the wall or dividing streamline, m (Fig. 1)
y_c = radial distance from the wake centerline, m (Fig. 1)
α_R = coefficient of resistivity, V/K
β = Falkner–Skan pressure gradient parameter [Eq. (9)]
γ = ratio of specific heats (c_p/c_v)
η = Howarth and Levy's transformation parameter [Eq. (11)]
μ = viscosity, kg/(m · s)
ρ = density, kg/m^3
τ_{est} = nondimensional flow establishment parameter [Eq. (30)]
τ_w = shear stress at the wall ($\mu[\mathrm{d}u/\mathrm{d}y]_w$)

Subscripts

b = base (Fig. 1)
d = dividing streamline
e = outer edge of boundary layer
eq = equilibrium
est = flow establishment
o = total conditions
r = reattachment point (Fig. 1)
sep = separation point
stag = front stagnation point (Fig. 1)
w = body/wall
1 or ∞ = conditions ahead of bow shock/freestream (Fig. 1)
2 = conditions behind bow shock (Fig. 1)
3 = inviscid flow outside free shear layer (Fig. 1)
4 = inviscid flow behind wake recompression shock (Fig. 1)

I. Introduction

IN DESIGNING space probes for planetary entry, an understanding of the aerothermodynamics behind the body in various atmospheres is essential. Usually, these probes travel at superorbital speeds (i.e., flight speed above 8 km/s or total specific enthalpy over 30 MJ/kg [1]), and they are shaped as blunt bodies to reduce excessive heating rates. Figure 1 illustrates a schematic of the near wake behind a blunt body.

The near-wake region as defined in this paper extends from the body shoulder to the reattachment point. For blunt bodies that are having a fixed separation point, it is often assumed that the incoming boundary layer separates at the body shoulder, which then forms a free shear layer as the flow detaches from the body surface.

Received 28 September 2009; revision received 25 February 2010; accepted for publication 14 March 2010.

*Graduate Student, Australian Defence Force Academy, School of Engineering and Information Technology.

†Visiting Senior Research Fellow, Australian Defence Force Academy, School of Engineering and Information Technology. Associate Fellow AIAA.

‡Senior Lecturer, Australian Defence Force Academy, School of Engineering and Information Technology. Senior Member AIAA.

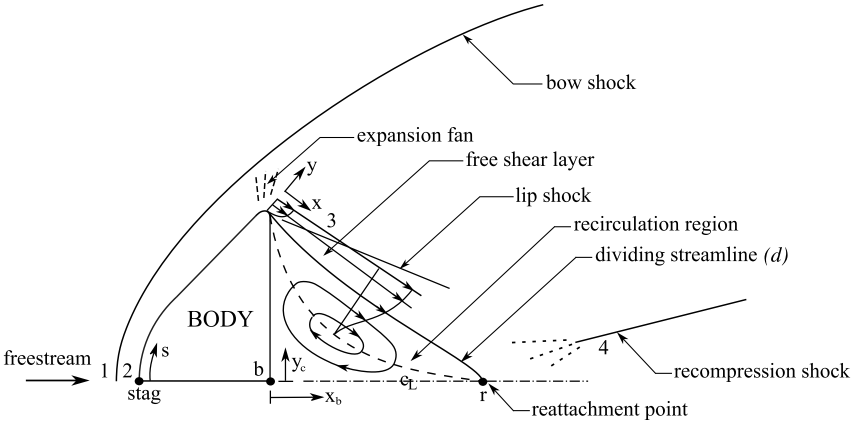

Fig. 1 A schematic of the near wake behind a blunt body.

The dividing streamline then separates the flow, which continues to flow downstream of the reattachment point from that which turns back and recirculates.

The aerothermodynamics behind various blunt bodies have been examined for planetary entry conditions for a broad range of atmospheres, but previous experimental studies have been limited to suborbital speeds (see, for example, [2,3]). The flow enthalpies at which these data were obtained are not high enough to match the flow conditions that are usually encountered in real flights. Also, the available experimental data are limited to those conducted using a side or a rear sting ([2,4]), which can severely disturb the flow structure in the near wake. At present, there is no reliable superorbital experimental data behind a blunt body that represents more realistic flow conditions at sufficiently high enthalpies.

Herein, we describe the experiments conducted in the X2 expansion tube (which is located at the University of Queensland in Australia) to investigate the aerothermodynamics behind a blunt body at superorbital speeds. The model that was investigated is a 45° half-angle blunted cone with a flat base and bluntness ratio (n) of 0.5. It was suspended by thin wires. The forebody profile of the model is equivalent to the Mars microprobe configuration of [3].

Two flow conditions were investigated: one in air and the other in a Martian atmosphere ($96\%CO_2$-$4\%N_2$). The total specific enthalpies for the conditions were 44.5 and 32.9 MJ/kg, and the freestream velocities were 8.3 and 8.1 km/s for air and CO_2-N_2, respectively.

For this study, particular emphasis was placed on the effect of chemistry on the near wake. The experimental data, such as the surface pressure and heat flux, are compared with the numerical results that were obtained using the multiblock compressible Navier–Stokes solver (MBCNS), which includes the finite-rate chemistry. These results are then compared with a theory that is based on perfect gas. This theory was initially developed by Denison and Baum [5] for a slender body with a blunt base, and it was successfully extended by Park et al. [6] to flows behind a two-dimensional blunt body, such as a cylinder at speeds from 2.6 to 4.6 km/s. The corresponding enthalpies varied from 4 to 13.4 MJ/kg. Herein, for the first time, the validity of using this theory for axisymmetric blunt bodies in high-enthalpy superorbital flows is examined.

Section II details the experimental facility, models, sensors, and flow conditions that were used in the X2 expansion tube experiments. Section III discusses the computational method used for blunted-cone simulations. Details regarding the computational solver and results from the grid independence study are then presented. In Sec. IV, the laminar near-wake theory that is capable of predicting base pressure and base heat flux of blunt bodies is presented. In Sec. V, the numerical and theoretical results are compared and validated with the measured data. The summary and conclusions are then presented in Sec. VI.

II. Experimental Details

A. X2 Expansion Tube

The experiments were conducted using the X2 expansion tube, which is located at the Centre for Hypersonics, University of Queensland, Australia. This facility is capable of producing superorbital flow conditions by using the enthalpy multiplication mechanism of the unsteady expansion process. A schematic of the X2 expansion tube is shown in Fig. 2.

The facility is approximately 20 m long, and it is driven by a 35 kg single-stage piston [7,8]. Upon the release of the piston, the pressure of the driver gas in the compression tube exceeds the burst pressure of the primary diaphragm (1.2 mm cold-rolled steel), causing it to rupture. This then creates the primary shock wave, which propels the test gas in the shock tube.

The arrival of the primary shock at the end of the shock tube causes the rupture of the light secondary diaphragm (6 μm thin Mylar), which initially separates the test gas from the acceleration gas. The compressed test gas is then processed by an unsteady expansion,

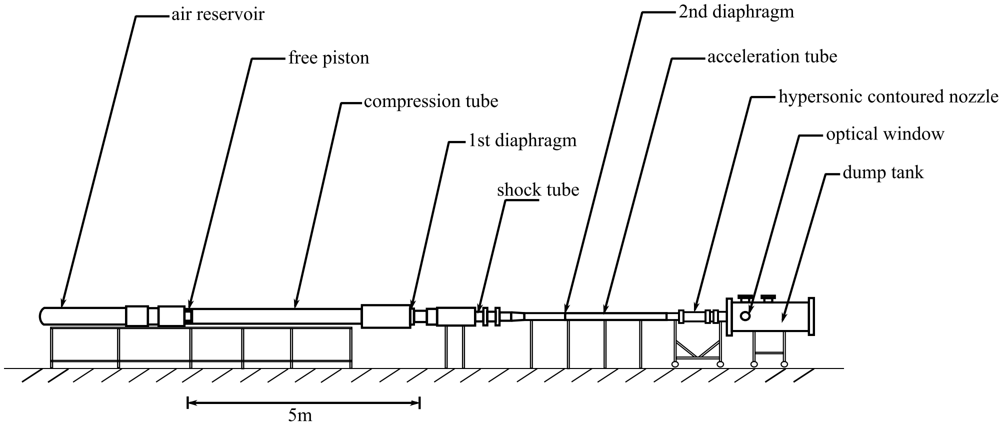

Fig. 2 A schematic of the X2 expansion tube.

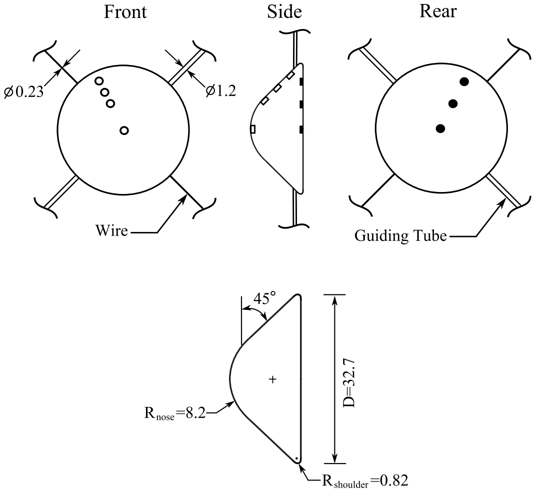

Fig. 3 A schematic of the model. (○ denotes thermocouples, and ● denotes thin-film gauges. All dimensions are in mm.)

which begins to expand into the acceleration tube, generating the secondary shock wave. The acceleration gas further expands through the hypersonic contoured nozzle and reaches the model. The nozzle had an exit diameter of 208 mm, and the length was 1.4 m. The usable test core at the nozzle exit was approximately 80–100 mm, and the duration of steady periods was approximately 100 μs for the present flow conditions. Further details regarding the theory and operation of the X2 expansion tube are found in [9].

B. Model Details

The 45° half-angle blunted-cone model was used for the present experiments. It was manufactured from steel, and it had a diameter of 32.7 mm, with a flat base. The forebody profile of the model was equivalent to a Mars microprobe [3]. The model was mounted using four wires, 90° apart from each other, and it was located at the nozzle exit, facing parallel to the flow (zero angle of attack). The diameter of the wires was 0.23 mm. The leads connected to the sensors inside the model were electrically insulated and covered by two guiding tubes, which had a diameter of 1.2 mm. Figure 3 shows a schematic of the model with corresponding sensor locations. It is to be noted that, out of four wires, two wires were placed inside of the guiding tubes.

As shown in Fig. 3, the present model uses relatively thick guiding tubes that could considerably disturb the flow structure in the near wake [10]. However, it was necessary to ensure that all the wirings connected to the sensors inside of the model were taken outside of the expansion tube. Furthermore, optical data and numerical results of Hruschka et al. [11] on a similar model revealed that, although the use of the 1.2-mm-diam guiding tubes somewhat disturbed the flow structure, their effects on the near wake were not too severe.

The surface heat flux around the forebody was measured using K-type surface junction thermocouples. The K-type thermocouples were chosen for the forebody heat flux study, as they are quite robust and have relatively fast signal responses. Each of them consisted of a chromel wire fitted coaxially within a hollow cylinder of alumel. The outer diameter of each thermocouple was 2 mm, with a length of 5 mm. Sandpapers were used to form a junction, resulting in tiny strands between the ends of dissimilar metals. The resistance of junctions was approximately 1.4 Ω, and the sensitivity of the thermocouple was found to be 40 $\mu\mathrm{V/K}$ at room temperature [12].

In the base, the surface heat flux was measured using thin-film gauges. It consisted of thin films of platinum, which were applied to the surfaces of Macor substrate that had negligible thermal conductivity. The diameter of the Macor was 2 mm, and its length was 4 mm. Detailed descriptions of the manufacturing of the gauges can be found in [13]. The thin-film gauges were chosen to measure the surface heat flux in the base region, due to the nature of flow and the fact that thin films have a much higher signal-to-noise ratio than thermocouples.

The surface heat flux is based on the time history of temperature, which can be calculated using the relation [12],

$$q(t_n) = \frac{2(\rho c_p k)^{1/2}}{\pi^{1/2}} \sum_{i=1}^{n} \frac{T(t_i) - T(t_{i-1})}{(t_n - t_i)^{1/2} + (t_n - t_{i-1})^{1/2}} \tag{1}$$

where $T(t_i) = V(t_i)/\alpha_R$ and $(\rho c_p k)^{1/2}$ are known as the thermal products of the substrate. The thermocouples were calibrated using a water dipping technique [14], and $(\rho c_p k)^{1/2}$ was determined to be $9690 \pm 300\ \mathrm{Ws^{0.5}/m^2K}$. For thin-film gauges, $(\rho c_p k)^{1/2}$ was determined to be $1500 \pm 120\ \mathrm{Ws^{0.5}/m^2K}$ through the dynamic calibration using a shock tunnel, and the coefficient of resistivity α_R was found to be $1.52 \pm 0.08\ \mathrm{mV/K}$ through the static calibration using a furnace. The typical resistances of the gauges were 120–150 Ω. Detailed descriptions regarding the gauge calibration can be found in [13,15].

Concerning the size of the model, only two surface pressures were measured. One was measured at the front stagnation point and the other at the center of the base. The surface pressure at the center of the base was measured using a XCS-093-series Kulite pressure transducer. It was capable of measuring the pressures in the range of 0 to 34.5 kPa. The transducer had a diameter of 2.4 mm, and its length was 9.5 mm. The sensitivity of the sensor was $3.66 \pm 0.044\ \mathrm{mV/kPa}$. The sensor was flush mounted. The front stagnation pressure was measured using a 113M165-series PCB Piezotronics pressure transducer. It had a sensitivity of 7.48 mV/kPa. The transducer was cavity mounted, with a diameter of 1.4 mm and a depth of about 1 mm.

C. Flow Conditions

Two flow conditions were investigated: one in air (75.5%N_2-23.2%O_2-1.3%Ar) and the other in a Martian atmosphere (96%CO_2-4%N_2). The flow conditions were obtained by simulation, using a Lagrangian one-dimensional code, L1d, which is an in-house code from the University of Queensland. The chemical reactions were incorporated in the code. The L1d is known to be capable of simulating transient flow conditions in facilities, such as light gas launchers, free-piston-driven shock tunnels, or expansion tubes (for example, see [8,15,16]). The code produces solutions to a second-order accuracy in both space and time. Also, it is able to capture and model the nonlinear effects, such as an attenuation of the shock speed in the acceleration tube [8].

The chemical reactions used for the flow simulation are shown in Table 1. The reaction rates were taken from [17] for air and [18] for CO_2-N_2.

Where $M_1 = $ O, N, O_2, N_2, NO; $M_2 = $ O, O_2, N_2, NO; and $M_3 = $ N, O, N_2, O_2, CO, NO, CO_2 are the third-body reaction species.

For the flow simulation, thermal equilibrium was assumed, and the gas was treated as a mixture of thermally perfect species. Viscosity and thermal conductivity of the gas were calculated using the curve-fitted expressions by NASA's CEA (chemical equilibrium with applications) program [19]. Concerning previous studies that noted radiation and ionization effects are not so strong at similar flow conditions to the present study (see, for example, [7,15,20–22]), it was assumed that no ionized species would be present in the flow, and the radiation effects were neglected in the calculations.

Table 1 List of chemical reactions

No.	Air	CO_2-N_2
1	$N_2 + M_1 \rightleftharpoons N + N + M_1$	$N_2 + M_3 \rightleftharpoons N + N + M_3$
2	$O_2 + M_2 \rightleftharpoons O + O + M_2$	$O_2 + M_3 \rightleftharpoons O + O + M_3$
3	$N_2 + N \rightleftharpoons 2N + N$	$NO + M_3 \rightleftharpoons N + O + M_3$
4	$NO + M_2 \rightleftharpoons N + O + M_2$	$CO_2 + M_3 \rightleftharpoons CO + O + M_3$
5	$NO + O \rightleftharpoons O_2 + N$	$N_2 + O \rightleftharpoons NO + N$
6	$N_2 + O \rightleftharpoons NO + N$	$NO + O \rightleftharpoons N + O_2$
7	——	$CO_2 + O \rightleftharpoons O_2 + CO$

Table 2 Flow conditions

		Air	±%	CO_2-N_2	±%
Nozzle exit	T_∞, K	3570	3.0	2790	8.3
	p_∞, kPa	2.5	6.2	1.7	20.3
	u_∞, km/s	8.3	1.4	8.1	4.0
	H_o, MJ/kg	44.5	2.8	32.9	10.4
	M_∞	6.1	0.2	8.1	1.0
	ρ_∞, kg/m^3	0.0018	8.7	0.0022	16.9
	p_{pitot}, kPa	104	6.0	136	22.2
	Re_∞, 1/m	1.4×10^5	4.9	2.0×10^5	7.3
	γ	1.38	0.2	1.27	0.3
	Mass fractions N_2	0.682	3.0	0.033	0.8
	O_2	0	0	0.177	8.9
	NO	0.00024	9.5	0.015	6.2
	O	0.232	2.7	0.073	31.7
	N	0.0723	19.7	0	0
	Ar	0.013	0	0	0
	CO_2	0	0	0.251	15.9
	CO	0	0	0.451	4.3
Shock tube	Shock speed, km/s	4.8	1.6	4.8	6.8
Acceleration tube	Shock speed, km/s	9.2	2.0	8.8	5.8

Table 2 summarizes the present flow conditions that were computed using the L1d. The uncertainties (±%) were based on the 95% confidence interval. The measured pitot pressures (p_{pitot}) and shock speeds agreed with the calculated values within 4 and 10%, respectively.

In view of the high Mach numbers and moderate Reynolds numbers, the flows were considered laminar. Also, the characteristic unsteadiness usually associated with transitional and turbulent flows was not observed from both surface pressure and heat flux signal traces.

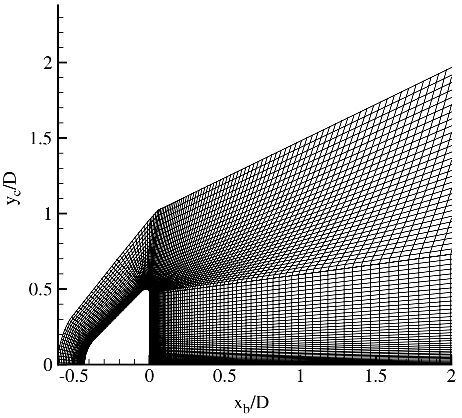

Fig. 4 Computational grid of the model (7560 cells).

III. Computational Method

A. Multiblock Compressible Navier–Stokes Solver

For the present study, the MBCNS (which is an in-house code from the University of Queensland [23]) was used to model the hypervelocity flow around the blunt body. The code performs a time integration of the Navier–Stokes equations for two-dimensional (planar or axisymmetric) bodies, using a cell-centered finite-volume formulation. Also, it uses a multiple-block structured mesh, and it has a shock-capturing capability through the use of a limited reconstruction scheme [1]. The mass, momentum, energy, and species flux between finite-volume cells were calculated using an advection upwind splitting method [24].

The simulations were performed for both nonreacting and reacting flows. The freestream conditions that were obtained using the L1d were used as the inflow conditions for the blunt-body simulation. The nonreacting flows were treated as in a chemically frozen state. For the reacting flows, the chemical reactions that were used for the L1d flow simulation were again used. The surface temperature of the model was assumed to be at 296 K. It was assumed that the surface was nonablative and noncatalytic. The steady states were assumed to have been reached when the simulated flow properties, such as pressure, velocity, and temperature, plateau to their constant values.

B. Grid Independence

The grid independence was studied using three different grid sizes. The total grid sizes used for this study were 3340, 7560, and 13,320 cells. Figure 4 shows the computational grid of the case that had 7560 cells.

Considering that the reacting gas simulation with a fine mesh usually takes a considerable amount of time, the grid independence study was only made for the nonreacting gas. The sensitivity of surface quantities on grids, such as the pressure and heat flux, is shown in Fig. 5. In the figures, the pressure is normalized with respect to the freestream pressure, and the heat flux is expressed in terms of the freestream Stanton number:

$$St_\infty = \frac{q_w}{\rho_\infty u_\infty (H_o - H_w)} \tag{2}$$

From Fig. 5, it is evident that the simulated surface pressures are quite insensitive to the grid size on the forebody. The simulated surface heat fluxes, however, show some changes, but the level of changes is still quite small. On the base, the differences seem quite noticeable between 3340 cells from others. These differences, then, become weak as the flow reaches the center of the base.

Figure 6 compares the steady total enthalpy contours in the base region between 7560 and 13,320 cells for air, which confirms that the differences between 7560 and 13,320 cells are indeed small. The results were similar for CO_2-N_2.

It is seen that, in most of the base region, the differences in total enthalpy between the two cases are quite small. There is some discrepancy along the wake centerline, but it still does not seem large. Taken together from the results in Figs. 5 and 6 (hence, in the

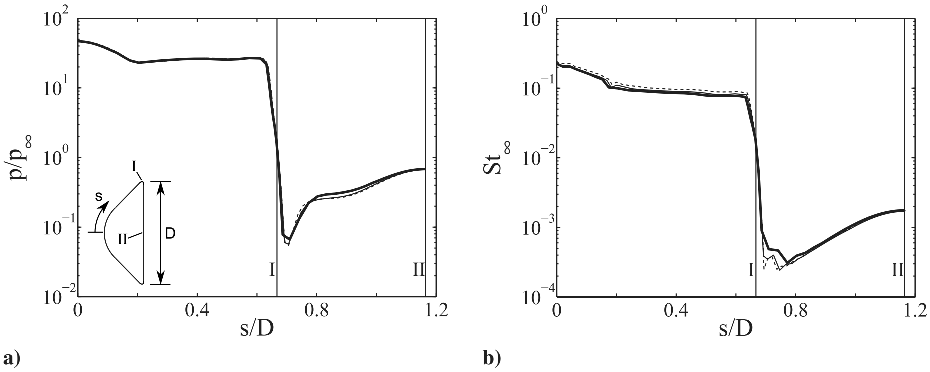

a) b)

Fig. 5 Sensitivity of surface quantities on grids: a) pressure and b) heat flux. (Thick lines denote 3340 cells, dashed lines denote 7560 cells, and thin lines denote 13,320 cells.)

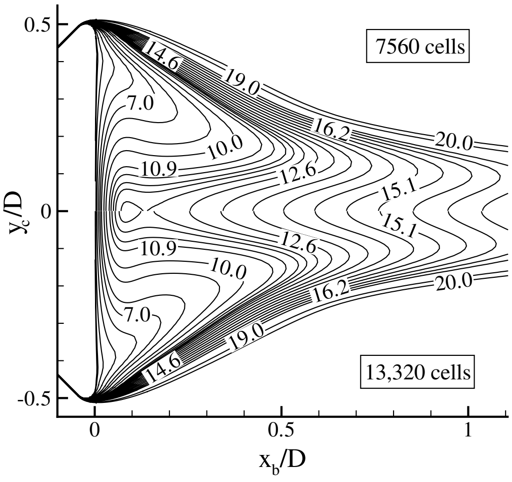

Fig. 6 Total enthalpy contours in the base region. Contour numbers represent MJ/kg.

rest of this paper), the numerical results that were computed using 7560 cells are presented.

IV. Analytical Approach to the Calculation of Base Pressure and Heat Flux

Recently, Park et al. [6] investigated the analytical approach to the calculation of base pressure and heat flux behind a blunt body, such as a circular cylinder at hypersonic speeds. They extended the theory of Denison and Baum [5] and Baum et al. [25], which was based on the framework of Chapman [26] and Chapman et al. [27], to make it suitable for blunt bodies. This included using more realistic separation profiles at a flow separation point rather than using the Blasius profile as an initial profile. Also, the energy balance equation, as was used in Baum et al. [25], was rearranged and applied to the high-enthalpy experimental conditions.

In this paper, the approach, as was used in Park et al. [6], for the calculation of base pressure and heat flux is again used but at much higher enthalpies. The equations were rearranged to be suitable for axisymmetric bodies [see Eqs. (10), (11), (15), (25), (26), and (29)]. For the enthalpies considered in [6] (approximately 4 to 13.4 MJ/kg for air), the real gas effects on surface quantities in the near wake were weak. For the present study, the enthalpies were increased to sufficiently high values (44.5 and 32.9 MJ/kg for air and CO_2-N_2, respectively) at which the chemical reactions in the near wake are believed to be strong.

A. Free Shear Layer

As noted in [5,6,25], the calculation of base pressure and heat flux behind the slender and blunt bodies require the computation of the free shear layer. To initiate the computation, the calculation of an initial profile (separation profile) is required. The equations that are required for the calculation of an initial profile can be obtained by transforming the boundary-layer equations through the Howarth–Dorodnitsyn's transformation [28]:

Momentum equation:

$$(Cf'')' + ff'' - \beta\{f'^2 - [(1-t_w)\theta + t_w]\} = 0 \tag{3}$$

Energy equation:

$$\left(\frac{C}{Pr}\theta'\right)' + f\theta' + \left(1 - \frac{1}{Pr}\right)\frac{C}{(1-t_w)}\left(\frac{u_e^2}{H_e}\right)[f'f''' + f''^2] = 0 \tag{4}$$

where

$$f' = u^* = \frac{u}{u_e} \tag{5}$$

$$\theta = \frac{H - H_w}{H_e - H_w} \tag{6}$$

$$t_w = \frac{T_w}{T_o} \tag{7}$$

$$C = \frac{\rho\mu}{\rho_e\mu_e} \tag{8}$$

$$\beta = \frac{2S_w}{u_e}\frac{\mathrm{d}u_e}{\mathrm{d}S_w}\left(\frac{T_o}{T_e}\right) \tag{9}$$

$$S_w = \int_0^s C\rho_e u_e \mu_e y_c^2 \,\mathrm{d}s \tag{10}$$

C is the Chapman–Rubesin constant, β is the modified Falkner–Skan pressure gradient parameter, and S_w is the reduced streamwise distance evaluated for the body. In solving Eqs. (3) and (4), the flows were assumed to be separated at the body shoulder. The corresponding thermodynamic properties at the edge of the boundary layer at the body shoulder were calculated using the isentropic relations. The pressure ratios and the ratio of specific heats required for this calculation were obtained from the present numerical results of reacting gas. The primes in Eqs. (3) and (4) denote differentiation with respect to η, where η is the normal distance parameter defined in terms of the Howarth and Levy's transformation, as in [5,6,25,28]:

$$\eta = \frac{\rho_e u_e}{(2S_w)^{1/2}}\int_0^y y_c \frac{\rho}{\rho_e}\,\mathrm{d}y \tag{11}$$

Equations (3) and (4) were solved using a multiple shooting method [29] through a fourth-order Runge–Kutta scheme, and then they were iterated until the following boundary conditions were satisfied at

$$\eta \to 0; \qquad f' = 0; \qquad \theta = 0; \qquad f_w = \text{const}$$

at

$$\eta \to \infty; \qquad f' = 1; \qquad \theta = 1$$

The equations were solved for the interval $0 \le \eta \le 7$, with 1000 node points across η. The iterations were terminated when $[f'(\infty) - 1] \le 1\mathrm{e}^{-5}$ and $[\theta(\infty) - 1] \le 1\mathrm{e}^{-5}$. The convergence of solutions was checked by doubling the size of η, and it was found that the differences were negligible.

Once the initial profiles (velocity and enthalpy) are calculated, the free shear layer computation can be initiated. In the computation of free shear layer, it is assumed that the Lewis and Prandtl numbers were assumed to be unity, and the pressure gradient in the free shear layer was assumed to be negligible in order to uncouple the momentum and energy equations, as in [5,6,25]. After applying the Howarth and Levy's transformations, the boundary-layer equations that govern the flow in the free shear layer become, after Denison and Baum [5],

Momentum equation:

$$u^*\frac{\partial F}{\partial CS} = F^2\frac{\partial^2 F}{\partial u^{*2}} \tag{12}$$

Energy equation:

$$u^*\frac{\partial H}{\partial CS} = F^2\frac{\partial^2 H}{\partial u^{*2}} \tag{13}$$

where

$$F = \frac{\partial u^*}{\partial Y} \tag{14}$$

$$Y = \rho_e u_e \int_0^y y_c(\rho/\rho_e)\,\mathrm{d}y \tag{15}$$

$$S = \int_0^x C\rho_e u_e \mu_e y_c^2\,\mathrm{d}x \tag{16}$$

$F(S, u^*)$ is a shear function, $H(S, u^*)$ is the total enthalpy, Y is the transformed normal distance, S is the reduced streamwise distance measured from the flow separation point (body shoulder), and u^* is defined in Eq. (5). In solving Eq. (13), H was replaced by a nondimensional enthalpy function W, where

$$H_e - H = (H_e - H_w)W + (H_e - H_c)(W_0 - W) \tag{17}$$

Here, H_c is the total specific enthalpy in the recirculation region, and $W_0 = [(H_e - H)/(H_e - H_w)]_{s=0}$ is the initial enthalpy function at the separation point.

Equations (12) and (13) were solved using a second-order-implicit finite-difference method [5]. The shear layer calculations were programmed using a commercialized software, MATLAB®, and 1000 mesh points were used for u^*. The convergence of solutions was checked by doubling the size of u^*, and it was found that the differences were negligible.

Once the shear layers were computed, the dividing streamline velocity ratio u_d^* was calculated using the relation [5],

$$u_d^* \frac{\mathrm{d}u_d^*}{\mathrm{d}S} = F_d \left(\frac{\partial F}{\partial u^*}\right)_d \tag{18}$$

Figure 7 presents the profiles of shear and enthalpy functions of the free shear layer for air and CO_2-N_2. It can be seen that the distributions of the shear, as well as the enthalpy functions, become flatter as S increases. As $S/S_w \to \infty$, the dividing streamlines for both the shear and the enthalpy functions tend to reach the Chapman limit and the dividing streamline ratio $u^* = 0.587$.

B. Base Pressure

The base pressure behind a blunt body may be expressed as

$$\frac{p_b}{p_{\mathrm{stag}}} = \frac{p_b}{p_{t2}} = \frac{p_b}{p_4} \times \frac{p_4}{p_{t4}} \times \frac{p_{t4}}{p_{t3}} \times \frac{p_{t3}}{p_{t2}} \tag{19}$$

In the calculation of Eq. (19), it is assumed that an isentropic inviscid flow assumption holds along the streamline at the outer edge of the boundary layer from the front stagnation point of the body through the shear layer, so that $p_{t3}/p_{t2} = 1$. The total pressure loss (p_{t4}/p_{t3}) was obtained using an oblique shock relation (the wake shock angles required for this were obtained from the present numerical results of reacting gas).

Assuming Chapman et al.'s isentropic recompression [27] at the reattachment point and constant pressure mixing [26] hold in the recirculation region,

$$\frac{p_t}{p_e} = \frac{p_4}{p_b} = \left[1 + \frac{(\gamma - 1)}{2} M_d^2\right]^{\gamma/\gamma-1} \tag{20}$$

where

$$M_d = u_d/\sqrt{\gamma R T_d} \tag{21}$$

According to Kubota and Dewey [30], the dividing streamline temperature ratio for isoenergetic flow can be expressed as

$$\frac{T_d}{T_e} = 1 + \frac{(\gamma - 1)}{2} M_e^2 (u_d^* - u_d^{*2}) \tag{22}$$

where T_d is the temperature in the recirculation region, and T_e is the external shear layer static temperature.

The pressure behind the wake recompression shock can be obtained using an isentropic inviscid flow relation,

$$\frac{p_{t4}}{p_4} = \left[1 + \frac{(\gamma - 1)}{2} M_4^2\right]^{\gamma/\gamma-1} \tag{23}$$

where M_4 can be expressed using a Chapman's relation [26],

$$M_4^2 = (1 - u_d^{*2}) M_e^2 \tag{24}$$

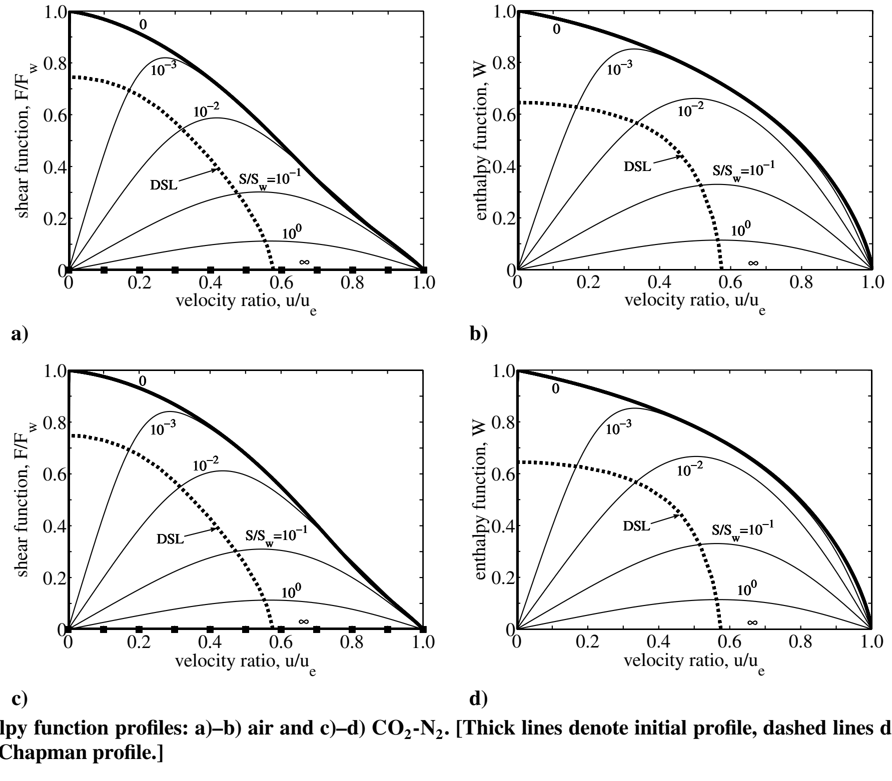

a) b) c) d)

Fig. 7 Shear and enthalpy function profiles: a)–b) air and c)–d) CO_2-N_2. [Thick lines denote initial profile, dashed lines denote dividing streamline (DSL), and ■–■ denote Chapman profile.]

C. Base Heat Flux

As noted in [25], the energy balance in the near wake is expressed as

$$\left[\begin{array}{c} E_{\text{in}} \\ -\int_0^\infty (H_e - H)\rho u\left(\frac{2}{\sqrt{3}}\pi y_c\right)\mathrm{d}y \end{array}\right]_{\text{sep}} = \left[\begin{array}{c} E_{\text{out}} \\ -\int_{y_d}^\infty (H_e - H)\rho u\left(\frac{2}{\sqrt{3}}\pi y_c\right)\mathrm{d}y \end{array}\right]_{x_r} + Q_b \qquad (25)$$

Here, E_{in} is the energy from the boundary layer that enters into the free shear layer at the flow separation point, E_{out} is the energy above the dividing streamline that travels downstream of the reattachment

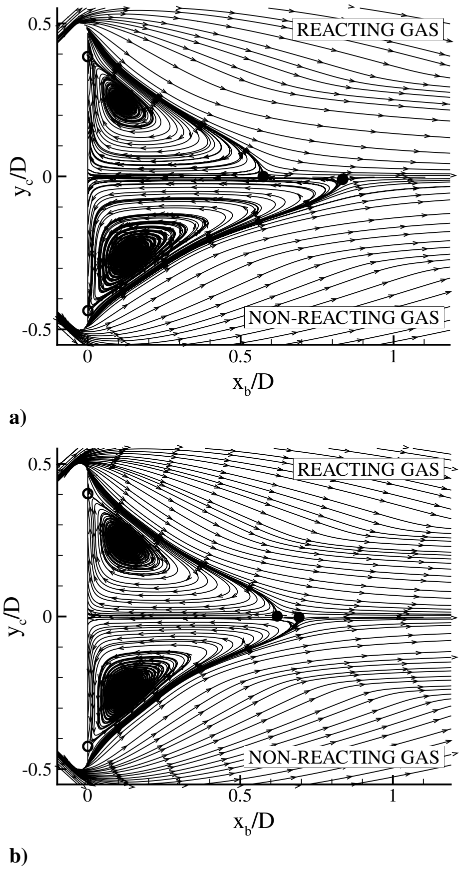

Fig. 8 Comparison of streamlines: a) air and b) CO$_2$-N$_2$. (○ denotes separation point, and ● denotes reattachment point.)

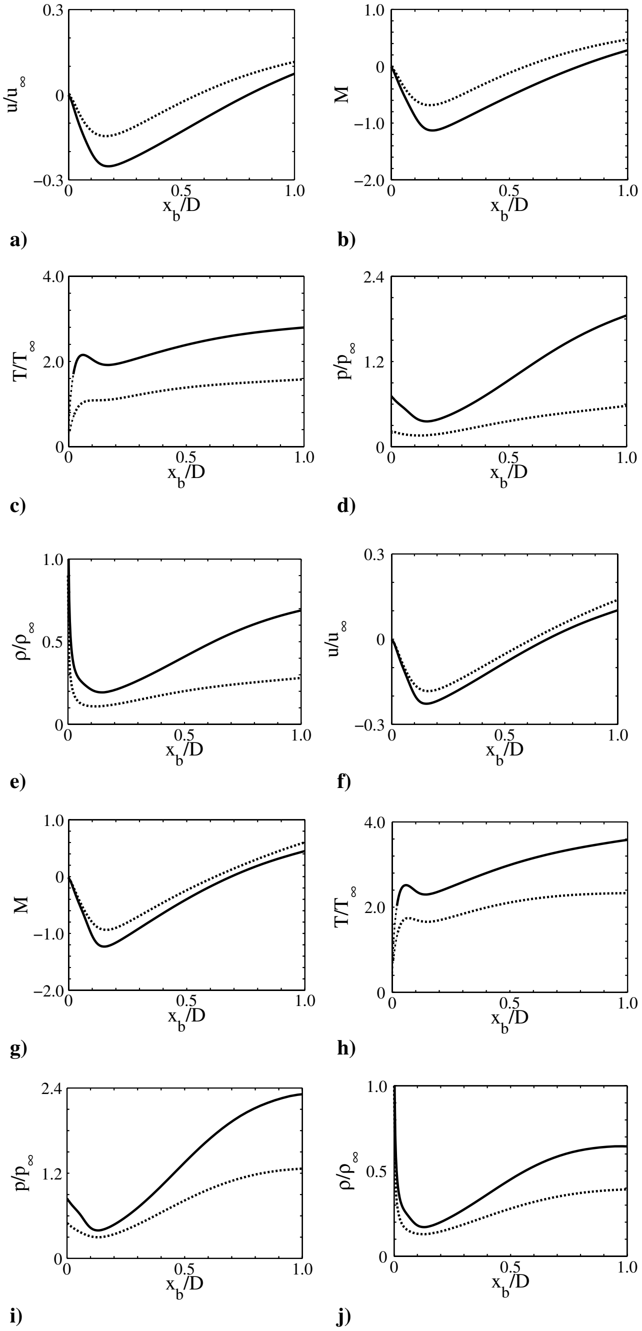

Fig. 10 Flow properties along the wake centerline: a)–e) air and f)–j) CO$_2$-N$_2$. (Lines denote nonreacting gas, and dashes denote reacting gas.)

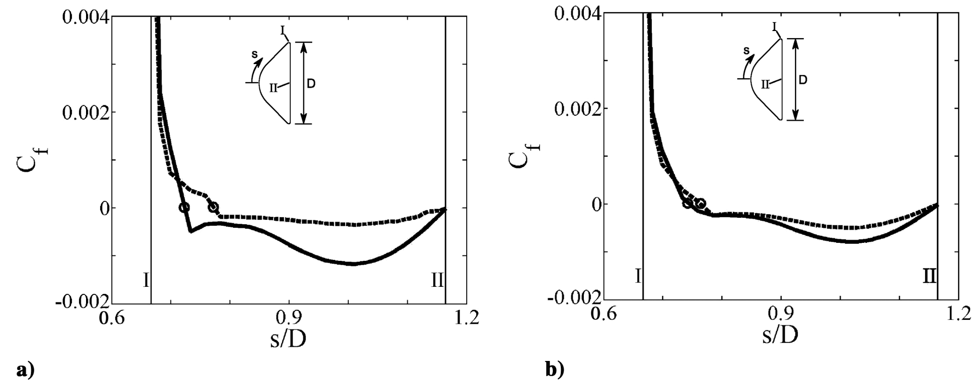

Fig. 9 Skin-friction coefficient: a) air and b) CO$_2$-N$_2$. (○ denotes separation point, lines denote nonreacting gas, and dashes denote reacting gas).

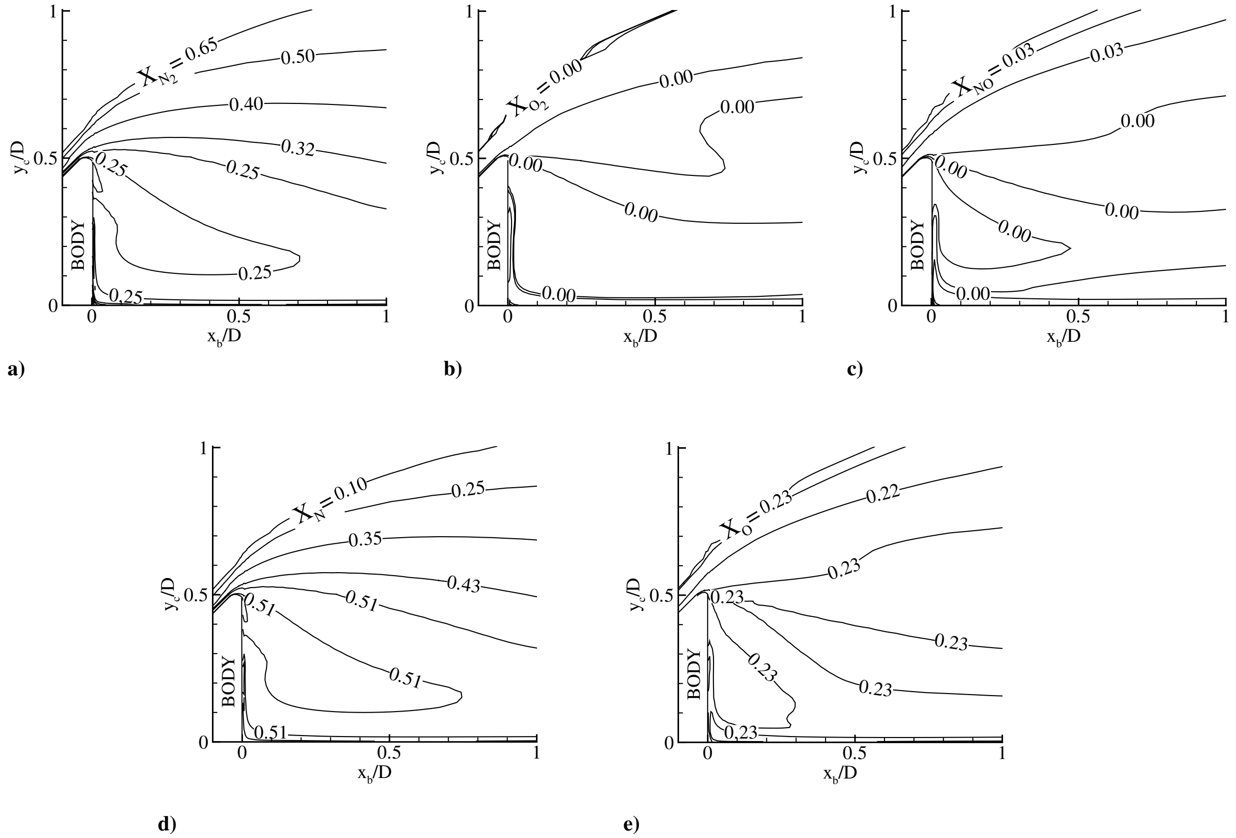

Fig. 11 Contours of species mass fraction in the near wake for air: a) N_2, b) O_2, c) NO, d) N, and e) O.

point, and Q_b is the total heat flux into the shear layer and the recirculation zone and to the base wall. $Q_b = q_b A$, where A is the base surface area. Equation (25) employs the Mangler transformation for an axisymmetric body.

The first integral E_{in} can be expressed by rearranging Eq. (11):

$$E_{\mathrm{in}} = \left[-\left(\frac{2}{\sqrt{3}}\pi\right)(2S_w)^{1/2}\int_0^\infty (H_e - H)u^*\,\mathrm{d}\eta\right]_{\mathrm{sep}} \tag{26}$$

The second integral E_{out} can be simplified by transforming the y coordinate to the u^* coordinate. Rearranging Eq. (15) and substituting it into Eq. (14) yields

$$\int_0^\infty \rho y_c\,\mathrm{d}y = \frac{1}{u_e}\int_0^{u_e^*}\frac{1}{F}\,\mathrm{d}u^* = \frac{1}{u_e}\int_0^1 \frac{1}{F}\,\mathrm{d}u^* \tag{27}$$

Since E_{out} is the energy integral from the dividing streamline to the outer edge of the free shear layer at the reattachment point,

$$\int_{y_d}^\infty \rho y_c\,\mathrm{d}y = \frac{1}{u_e}\int_{u_d^*}^1 \frac{1}{F}\,\mathrm{d}u^* \tag{28}$$

Substituting Eq. (28) into the second integral E_{out} of the energy balance yields

$$E_{\mathrm{out}} = \left[-\left(\frac{2}{\sqrt{3}}\pi\right)\int_{u_d^*}^1 (H_e - H)\frac{u^*}{F}\,\mathrm{d}u^*\right]_{x_r} \tag{29}$$

The base pressure and heat flux calculated from using the preceding expressions are next compared with the experimental data and numerical results.

V. Results and Discussion

A. Results of Numerical Calculations

The comparison of steady flow streamline plots for reacting and nonreacting gases is shown in Fig. 8.

It is evident that the steady vortex in the near wake for the reacting gas is smaller than that of the nonreacting gas. The difference in the size of the vortex is much more prominent in air than CO_2-N_2. In particular, with reacting air, the rear stagnation point (reattachment point) is approximately 27% closer to the base in comparison with the nonreacting case. In the case of CO_2-N_2, the difference is only 7%. This is quite unlike what was reported by Dogra et al. [31] who noted that, in their 70° half-angle blunted-cone (with a flat base) direct simulation Monte Carlo (method) (DSMC), the size of the vortex for the reacting gas was 25% larger than that of the nonreacting case behind a blunt body with air as test gas. Their results were obtained at lower velocity ($u_\infty = 7$ km/s) and much lower density ($\rho_\infty = 7.955 \times 10^{-6}$ kg/m^3) when compared with the present case.

Figure 9 shows the distributions of the skin-friction coefficient behind the base. From the figure, it is evident that the flow separation (where the skin friction goes to zero) actually occurs on the base and not at the shoulder. This is consistent with the numerical results of Grasso and Pettinelli [32] and Gorshkov and Lunev [33], who also observed that the separation point was on the base and that, the lower the Reynolds number, the lower its position.

Figure 9 also indicates that flow separation occurs later for reacting gas for both air and CO_2-N_2. It would, therefore, seem that, the lower the separation point on the base, the stronger the expansion at the shoulder and, consequently, the smaller the size of the recirculation region. This is also consistent with the results of Zhong et al. [22], who also noted that the size of the recirculation region with reacting gas, in their case, was smaller in contrast with the results obtained by Dogra et al. [31]. It should be noted that both Zhong et al. [22] and Dogra et al. [31] used the DSMC simulations while, in the present case, we have used Navier–Stokes-based computations. The differences between the values of the recirculation region lengths of Zhong et al. [22] and Dogra et al. [31] are attributed by Zhong et al. [22] to grid size, even though the model and flow conditions were identical. It is, therefore, possible that the differences between the values of the recirculation region in the present experiment and that

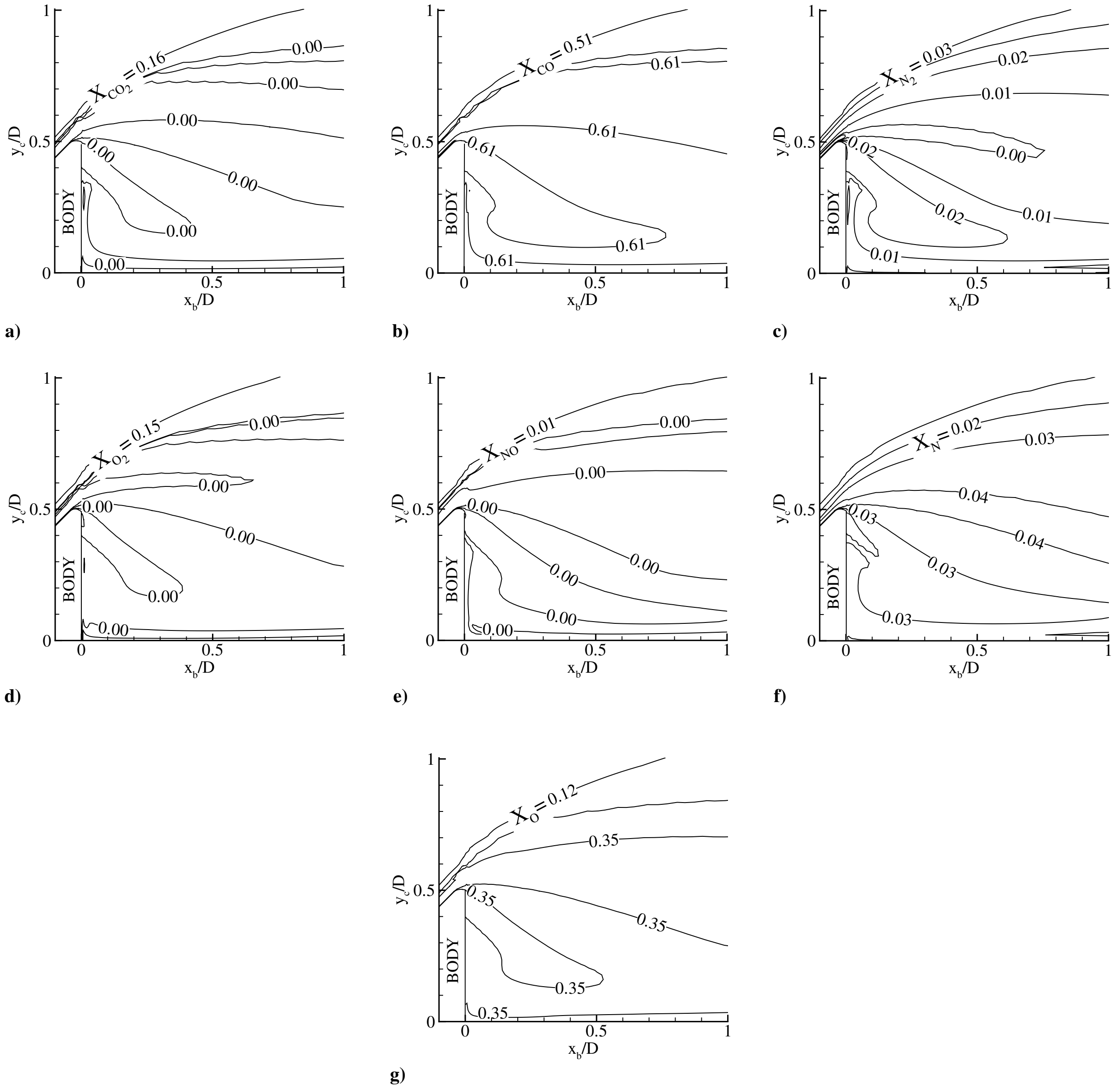

Fig. 12 Contours of species mass fraction in the near wake for CO_2-N_2: a) CO_2, b) CO, c) N_2, d) O_2, e) NO, f) N, and g) O.

of Dogra et al. [31] are a combination of model geometry, flow conditions, and method of computation.

B. Flow Properties Along the Wake Centerline

Figure 10 compares the flow properties along the wake centerline for the reacting and nonreacting cases. As is evident from the figures, the differences are quite considerable for both flow conditions. In Figs. 10b and 10g, negative Mach numbers correspond inside the recirculation region as the flow along the wake centerline in this region travels from the reattachment point to the base.

Concerning the Mach number distributions along the wake centerline, the maximum Mach number computed for the nonreacting gas is 65 and 31% higher than that of the reacting gas in the case of air and CO_2-N_2, respectively. It is also interesting to note that the maximum Mach number in the nonreacting case for both air and CO_2-N_2 are slightly supersonic and seem to occur at a distance of about $0.17D$ to $0.15D$ from the base. The rear stagnation point (where the Mach number is zero) seems to be at a distance of about $0.84D$ from the base for air and $0.69D$ for CO_2-N_2, respectively, in the nonreacting case. The corresponding values for reacting case are $0.57D$ and $0.62D$, respectively.

In their numerical studies, Grasso and Pettinelli [32], Gorshkov and Lunev [33], and Gnoffo [34] have all observed supersonic reverse-flow velocities in the recirculation region of a blunt body. The present data confirm this feature of the recirculating region behind blunt bodies in high Mach number flows.

This feature of high reverse-flow velocities in a recirculating flow has not often been commented on in the literature, as it is not always easy to measure in experiments. A few experimental studies that exist (for example, Panov and Shvets [35] and Martellucci et al. [36]), have measured centerline Mach numbers as high as 0.8 at high supersonic and moderate hypersonic freestream Mach numbers. Recently, Hruschka et al. [11,37], using planar laser-induced fluorescence velocimetry, have measured reverse-flow Mach numbers as high as 0.95 ± 0.15 along the axis in the recirculation region of a blunt body at Mach 10.

Also shown in Fig. 10 are the variation of pressure, velocity, density, and temperature. Concerning pressure, density, and temperature, they all show an increase as the base is approached. The fact that the temperature decreases as we approach very close to the base is due to the assumption made in the computation procedure regarding the surface boundary condition, which assumes the surface temperature to be 296 K. The increase in pressure, density, and

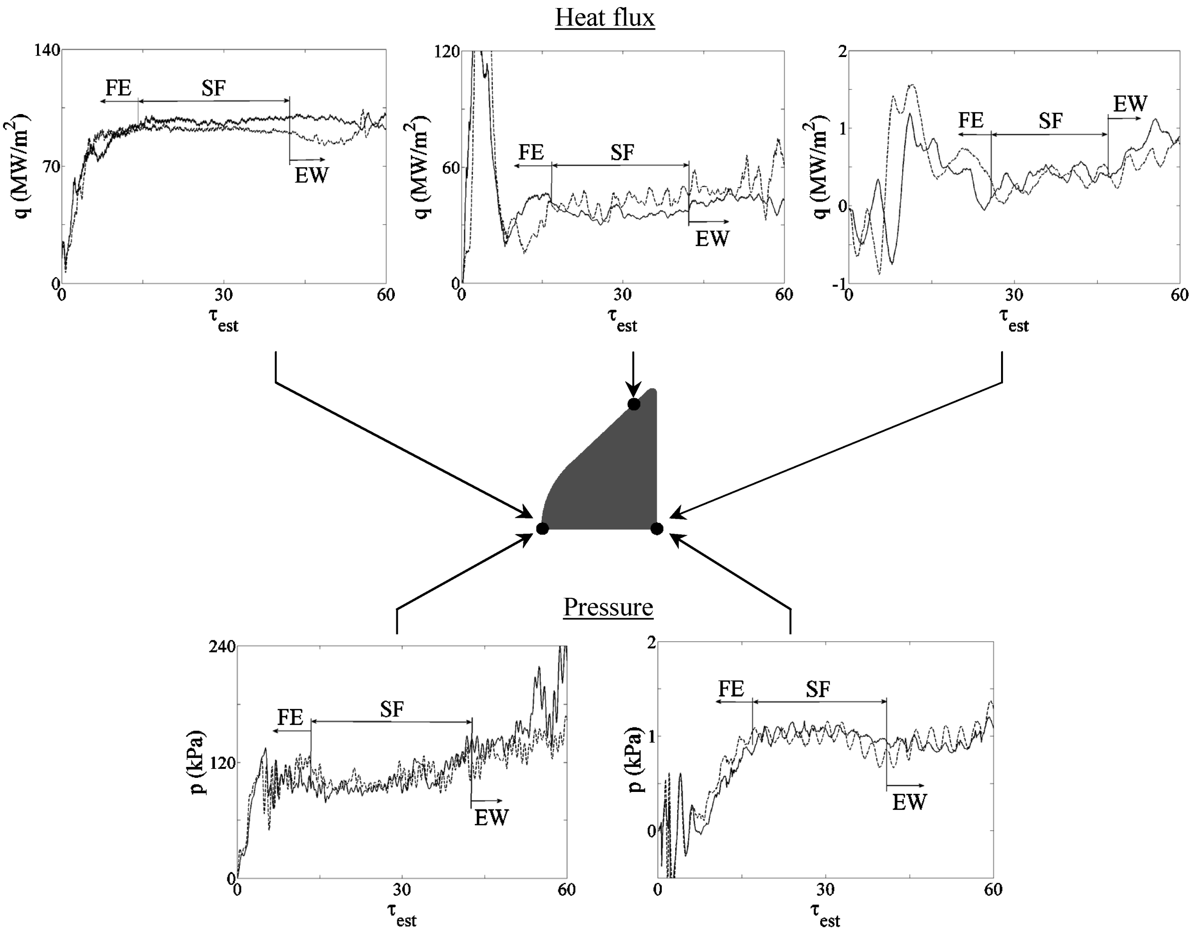

Fig. 13 Typical traces of surface pressure and heat flux at superorbital speeds for air (FE: flow establishment, SF: steady flow, EW: expansion wave).

temperature as the base is approached would suggest that the flow along the axis acts as a jet stagnating near the base. Such a phenomenon has been postulated by Panov and Shvets [35], based on experimental evidence. Then, in the presence of sonic or supersonic velocities, shocklets may very well appear. Presence of shocklets in supersonic shear layers has been hinted at in experiments by Papamoschou [38] and Smith and Dutton [39]. In the present instance, however, their presence could not be verified, as there were no visualization experiments performed.

Another point of note is that all the preceding flow parameters are not only lower for the reacting gas when compared with the nonreacting case, but their variations along the axis are more gradual.

C. Chemical Reactions in the Near Wake

Figures 11 and 12 show the contours of species mass fraction in the near wake for air and CO_2-N_2, respectively.

Figure 11 shows that all of the molecular oxygen (O_2) and nearly two-thirds of the molecular nitrogen (N_2) are dissociated before reaching the body surface in the recirculating region. At outer radial distances, the mass fraction of N_2 molecules gradually increases to the freestream value. Concerning the molecular oxygen, however, this trend could not be observed, because all oxygen is dissociated, even in the freestream. In the near wake, the highly dissociated N and O atoms could recombine to form NO molecules; but, in the present case, their formation seems negligible.

With regard to Fig. 11d, it is interesting to note that the dissociated molecular nitrogen in the forebody region near the surface seems to diffuse into the recirculating region. Results from Zhong et al. [22] show a similar state of affairs. Further, it is to be noted that there is no dissociation of N_2 molecules or recombination of N and O atoms that is occurring in this region, indicating that this region is essentially chemically frozen. Taken together, these results are qualitatively similar to those of Dogra et al. [31], although they were obtained at lower enthalpy and much lower density.

The contours of mass fraction in the near wake for CO_2-N_2 are shown in Fig. 12. The near wake consists of 61% of CO molecules, 35% of O atoms, 3% of N atoms, and about 1% of N_2 molecules.

As in the case of air, the CO_2-N_2 condition also shows the dissociated species, such as CO, O, and N atoms, in the forebody region near the surface, diffuse into the recirculating region, and this region is also chemically frozen. At outer radial distances, the mass fractions for CO_2 and O_2 molecules attain freestream values much faster than for the case of air. Once again, these results are qualitatively very similar to those obtained by Moss et al. [40] for a Mars Pathfinder model flying in a Martian atmosphere.

In the previous section, it was shown that the temperatures along the wake centerline for the nonreacting case were higher than that of the reacting case for both air and CO_2-N_2. It can be seen from Figs. 11 and 12 that this is because of the extensive amount of dissociated species in the flowfield of the near wake.

D. Experiments

1. *Flow Establishment*

Figure 13 shows the typical traces of surface pressure and heat flux at the front stagnation point, near the shoulder, and at the base for test gas air. The results were similar for CO_2-N_2. In the figure, τ_{est} is a nondimensional flow establishment parameter that can be expressed as [15,41,42]

$$\tau_{est} = \frac{tu_1}{D} \tag{30}$$

where t is the time after shock reflection, u_1 is the freestream velocity, and D is the model diameter. For the present study, the flows were considered to be steady when the mean values reached 95 and 90% of their final values for pressure and heat flux, respectively.

The steep gradients of the signals at the beginning of the flow were due to the shock arrival for both pressures and heat fluxes. The shock arrival is followed by the arrival of the acceleration tube gas and the test gas. The flow requires sufficient time to establish, and it then becomes steady. After the end of the steady period, unsteady expansion waves arrive and terminate the flow. The shot-to-shot variations of the signals for pressure and heat flux at the base during the steady flow were approximately ±15 and ±25%, respectively.

It can be estimated by Eq. (30) and Fig. 13 that, while the pressures required about 15 to 20 body lengths to establish steady flow behind the model, the heat fluxes required about twice as long to reach a steady state. This is consistent with the findings of [41,42], wherein flow establishment times of separated flow were investigated under low- to moderate-enthalpy conditions.

2. *Results and Comparison*

The effects of chemistry on surface quantities are presented in Figs. 14 and 15 for air and CO_2-N_2, respectively. In the figures, the error bars denote the experimental shot-to-shot variations of the averaged steady pressure and heat flux. The experimental data are compared with various theories, including the present theory as well as the numerical results that include the effects of chemistry. The forebody theories of Lees [43] and Fay and Riddell [44] were based on thermal equilibrium under an assumption of cold wall, where the surface heat flux was driven purely by thermal conduction.

Lees [43] gives the heat flux around the blunt body as

$$q_{\mathrm{eq}} \cong 0.5 Pr^{-2/3} (\rho_e \mu_e)_o^{0.5} u_1^{0.5} H_o F(s) \tag{31}$$

where

$$F(s) = \frac{(1/2^{0.5})(p/p_{\mathrm{stag}})(\mu T_o/\mu_o T)(u_e/u_1) y_c}{[\int_0^s (p/p_{\mathrm{stag}})(u_e/u_1)(\mu T_o/\mu_o T) y_c^2 \, \mathrm{d}s]^{0.5}} \tag{32}$$

For the front stagnation point, the expression of Fay and Riddell [44] has been used:

$$q_{\mathrm{stag,eq}} = 0.76 Pr^{-0.6} (\rho_w \mu_w)^{0.1} (\rho_e \mu_e)^{0.4} (H_e - H_w)(\mathrm{d}u_e/\mathrm{d}x)_{\mathrm{stag}}^{0.5} \tag{33}$$

In the calculations of Eqs. (31–33), the present numerical results of the reacting gas were incorporated to obtain the velocity gradient $(\mathrm{d}u_e/\mathrm{d}x)_{\mathrm{stag}}$ and the surface pressure distributions (p/p_{stag}). The isentropic flow relations were used to calculate the thermodynamic properties around the body, and Prandtl numbers were calculated using the curve-fit data of [45,46] for air and CO_2-N_2, respectively.

a. Forebody Data. In both Figs. 14 and 15, the forebody experimental heat fluxes agree closely with the numerical results of

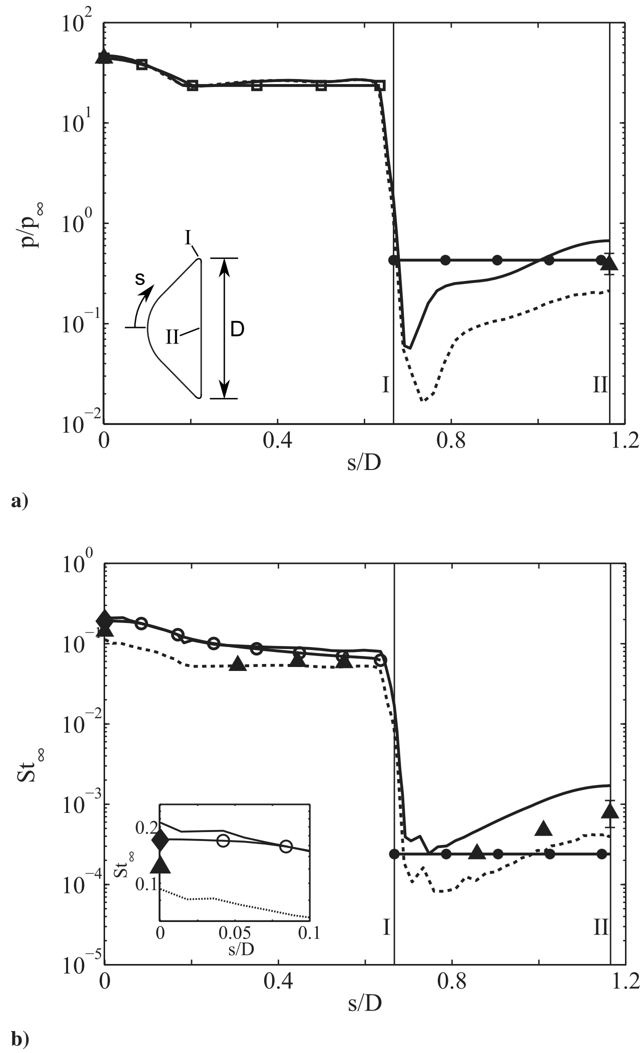

a)

b)

Fig. 14 Superorbital air data: a) pressure and b) heat flux. [▲ denotes present data (exp.), ◆ denotes theory (Fay and Riddell [44], front stagnation point heat flux), lines denote simulation (nonreacting gas), dashes denote simulation (reacting gas), ● denote present theory, ☐ denotes Newtonian theory (forebody pressure), and ○ denotes theory (Lees [43], forebody heat flux).]

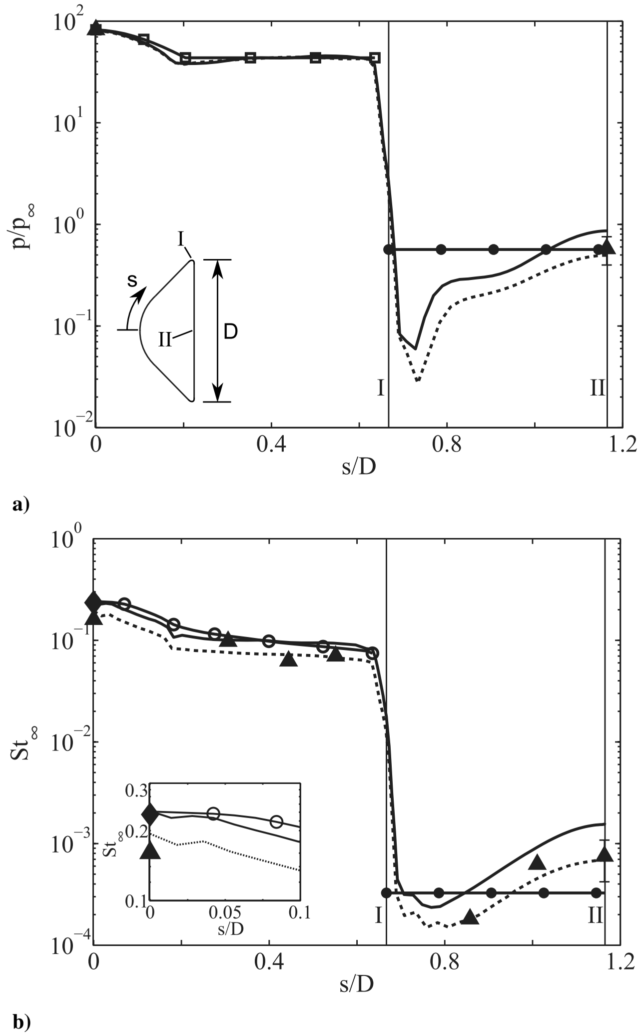

a)

b)

Fig. 15 Superorbital CO_2-N_2 data: a) pressure and b) heat flux. [▲ denotes present data (exp.), ◆ denotes theory (Fay and Riddell [44], front stagnation point heat flux), lines denote simulation (nonreacting gas), dashes denote simulation (reacting gas), ● denote present theory, ☐ denotes Newtonian theory (forebody pressure), and ○ denotes theory (Lees [43], forebody heat flux).]

the reacting gas. The numerical results for the front stagnation point heat flux of the nonreacting gas is 104 and 25% higher than that of the reacting gas for air and CO_2-N_2, respectively. The calculated heat fluxes using the theories of Lees [43] and Fay and Riddell [44] tend to overpredict the results when compared with the numerical results of the reacting gas, indicating the inadequacy of using them in high-enthalpy superorbital flows.

Unlike the surface heat fluxes, there are negligible differences between the numerical results of the reacting and nonreacting gases with regard to forebody pressures. The experimental pressures at the front stagnation point match quite well with the numerical results. It can also be seen that the forebody pressures calculated using the Newtonian theory are in good agreement with the numerical results.

b. Base Data. With regard to air, the experimental pressure and heat fluxes on the base lie in between the numerical results of reacting and nonreacting gases. For CO_2-N_2, however, the experimental data are in close agreement with the numerical results of the reacting gas.

There are some further notable features regarding both pressure and heat flux on the base. First, considering the pressure distribution on the base, both sets of data (reacting and nonreacting gases) show that there is a pressure minimum, after which there is a steep recovery. In his experiments on a cylinder in hypersonic flow, Dewey [47] points out that a pressure minimum indicates the point of separation. This has also been verified by Park et al. [6] in their experiments on cylinders in high-enthalpy hypersonic flows. It is seen from the results that the position of separation does not seem to vary much with CO_2-N_2, but it seems to separate much later for a reacting air. The constant pressure assumption normally made for the recirculation region behind a blunt base, therefore, seems not entirely true. It is also seen that, for both air and CO_2-N_2, the reacting gas values are much lower than the nonreacting case. The differences are somewhat greater with air.

The heat flux distribution shows a similar trend to that of pressure. Again, there is a minimum at the point of separation, and a recovery thereafter, up to the center of the base. As in the case of pressure, the location of separation for reacting and nonreacting air varies slightly but nearly same for reacting and nonreacting CO_2-N_2. Once again, the heat fluxes in the cases of both reacting air and CO_2-N_2 are lower than their nonreacting counterparts. As in the case of pressure, the differences with air are larger than CO_2-N_2. Compared with pressures, the heat flux distributions are somewhat shallower.

The theory, which is based on the assumption of constant pressure in the recirculation region behind the base, predicts the base pressure remarkably well, but it is not able to predict the pressure minimum at separation and the subsequent recovery. Similarly, the heat flux prediction is also fair but somewhat underpredicted when compared with the experiment and numerical calculations. The reason for this is that the calculations involve a number of assumptions, such as an idealized separation profile (the pressure ratios and the ratio of specific heats required for this calculation were obtained from the numerical results, as no measured data was available), constant pressure mixing, isentropic recompression, and a straight dividing streamline.

It should be pointed out that, in general, these distributions of surface quantities on both the forebody and the base are similar to those calculated for a 70° blunted cone in air, by Dogra et al. [31], using DSMC and Navier–Stokes simulations. However, they do not make any explicit comment on the separation location, although their data show that separation locations are slightly different for reacting and nonreacting air. However, the trend they show is different from the present, in that, in the reacting case, the separation is higher, rather than lower down, on the base. This would also be consistent with the earlier discussion about their finding that the reattachment with reacting air is 25% larger than the nonreacting case, in contrast to the present findings for air.

VI. Conclusions

The flow behind a 45° half-angle blunted cone in air and Martian atmospheres is investigated experimentally, numerically, and analytically at superorbital speeds. Particular emphasis was placed on the chemistry effects on the base and near wake. To the authors' knowledge, it is the first time that a fairly comprehensive set of experimental data on the base flow and near wake at superorbital speeds has been presented. The results may be summarized as follows.

The forebody experimental data of surface pressure and heat flux showed good agreement with the numerical results that included the effects of chemistry. The theories based on perfect gas and thermal equilibrium, such as those of Lees [43] and Fay and Riddell [44], tend to overpredict the data, showing the inadequacy of using them in such high-enthalpy superorbital flows.

Concerning the base, the results of the theory showed good agreement with the experiment and numerical calculations, as regards the base pressure. Similarly, the heat flux prediction was also fair but somewhat underpredicted. Both the experiment and numerical predictions showed a minimum and then gradual recovery in pressure and heat flux distributions on the base. The theory, which is based on constant pressure mixing in the wake, does not predict this.

With regard to air and CO_2-N_2, the numerical results indicate that the separation point is not located at the shoulder but, rather, down on the base. In the reacting case, the separation was lower than in the nonreacting case, thereby implying a stronger gas expansion near the shoulder region. This would then lead to a shorter recirculation region.

The present numerical results and the experimental data indicated that, at these high enthalpies, while the chemistry effects were seen to be strong in the near wake for the case of Martian atmosphere, their effect in the near wake for air was moderate.

Acknowledgments

This work forms part of the Physics of Base Flows of Planetary Entry Configurations project supported by the Australian Research Council, to whom grateful thanks are expressed. The authors also wish to express their thanks to R. G. Morgan for allowing the use of the X2 expansion tube facility and to T. Eichmann, A. Dann, C. Jacobs, D. Gildfind, and M. D'Souza for help in the running of the facility. Special thanks are due to D. Potter, who helped in the preparation of the input scripts in the running of the multiblock compressible Navier–Stokes solver simulation. At the University of New South Wales Australian Defence Force Academy, grateful thanks are due to F. Foppoli, who constructed the models, and to R. Hruschka and N. R. Deepak for helpful discussions.

References

[1] Wheatley, V., Chiu, H. S., Jacobs, P. A., Macrossan, M. N., Mee, D. J., and Morgan, R. G., "Rarefied, Superorbital Flows in an Expansion Tube," *International Journal of Numerical Methods for Heat and Fluid Flow*, Vol. 14, No. 4, 2004, pp. 512–537. doi:10.1108/09615530410532277

[2] Hollis, B. R., "Experimental and Computational Aerothermodynamics of a Mars Entry Vehicle," Ph.D. Thesis, North Carolina State Univ., 1996.

[3] Mitcheltree, R. A., Difulvio, M., Horvath, T. J., and Braun, R. D., "Aerothermal Heating Predictions for Mars Microprobe," *Journal of Spacecraft and Rockets*, Vol. 36, No. 3, 1999, pp. 405–411. doi:10.2514/2.3460

[4] Marvin, J. G., and Akin, C. M., "Pressure and Convective Heat-Transfer Measurements in a Shock Tunnel Using Several Test Gases," NASA TN D-3017, Sept. 1965.

[5] Denison, M. R., and Baum, E., "Compressible Free Shear Layer with Finite Initial Thickness," *AIAA Journal*, Vol. 1, No. 2, 1963, pp. 342–349. doi:10.2514/3.1535

[6] Park, G., Gai, S. L., and Neely, A. J., "Laminar Near Wake of a Circular Cylinder at Hypersonic Speeds," *AIAA Journal*, Vol. 48, No. 1, 2010, pp. 236–248. doi:10.2514/1.44167

[7] Scott, M. P., "Development and Modelling of Expansion Tubes," Ph.D. Thesis, Univ. of Queensland, 2006.

[8] Hayne, M. J., Mee, D. J., Gai, S. L., and McIntyre, T. J., "Boundary Layers on a Flat Plate at Sub- and Superorbital Speeds," *Journal of*

Thermophysics and Heat Transfer, Vol. 21, No. 4, 2007, pp. 772–779. doi:10.2514/1.26894

[9] Morgan, R. G., "Free-Piston Driven Expansion Tubes," *Handbook of Shock Waves*, edited by G. Ben-Dor, O. Igra, and T. Elperin, 1st ed., Academic Press, New York, 2001, pp. 603–622.

[10] Dayman, B., "Support Interference Effects on the Supersonic Wake," *AIAA Journal*, Vol. 1, No. 8, 1963, pp. 1921–1923. doi:10.2514/3.1958

[11] Hruschka, R., Park, G., Kleine, H., and O'Byrne, S., "Optical Investigation of Transient Phenomena in Hypersonic Shock Tunnels," *Proceedings of SPIE: The International Society for Optical Engineering*, Vol. 7126, 2008, Paper 71260J. doi:10.1117/12.823722

[12] Schultz, D. L., and Jones, T. V., "Heat Transfer Measurements in Short-Duration Hypersonic Facilities," AGARD AGARDograph 165, 1973.

[13] Kinnear, K., and Lu, F. K., "Design, Calibration and Testing of Transient Thin Film Heat Transfer Gauges," 20th AIAA Advanced Measurement and Ground Testing Technology Conference, Albuquerque, NM, AIAA Paper 98-2504, June 1998.

[14] Mallinson, S. G., "Shock Wave/Boundary Layer Interaction at a Compression Corner in Hyper-Velocity Flows," Ph.D. Thesis, Univ. of New South Wales, 1994.

[15] Hayne, M. J., "Hypervelocity Flow Over Rearward-Facing Steps," Ph.D. Thesis, Univ. of Queensland, 2004.

[16] Jacobs, P. A., "Shock Tube Modelling with L1d," Univ. of Queensland, Dept. of Mechanical Engineering, Rept. 13/98, Brisbane, Queensland, Australia, 1998.

[17] Gupta, R. N., Yos, J. M., Thompson, R. A., and Lee, K. P., "A Review of Reaction Rates and Thermodynamic and Transport Properties for an 11-Species Air Model for Chemical and Thermal Nonequilibrium Calculations to 30,000 K," NASA Rept. 1232, Aug. 1990.

[18] Park, C., Howe, J. T., Jaffe, R. L., and Candler, G. V., "Review of Chemical-Kinetic Problems of Future NASA Missions, II: Mars Entries," *Journal of Thermophysics and Heat Transfer*, Vol. 8, No. 1, 1994, pp. 9–23. doi:10.2514/3.496

[19] Gordon, S., and McBride, B. J., "Computer Program for Calculation of Complex Chemical Equilibrium Compositions and Applications. Part 1: Analysis," NASA Rept. 1311, 1994.

[20] Moss, J. N., and Price, J. M., "Survey of Blunt Body Flows Including Wakes at Hypersonic Low-Density Conditions," *Journal of Thermophysics and Heat Transfer*, Vol. 11, No. 3, 1997, pp. 321–329. doi:10.2514/2.6252

[21] Capra, B. R., Morgan, R. G., and Leyland, P., "New Gauge Design to Measure Radiative Heat Transfer to a Titan Aerocapture Vehicle in Expansion Tubes," *Proceedings of the Fifth European Symposium on Aerothermodynamics for Space Vehicles*, ESA, Cologne, Germany, Nov. 2004, p. 189.

[22] Zhong, J., Ozawa, T., and Levin, D. A., "Comparison of High-Altitude Hypersonic Wake Flows of Slender and Blunt Bodies," *AIAA Journal*, Vol. 46, No. 1, 2008, pp. 251–262. doi:10.2514/1.31056

[23] Jacobs, P. A., "MB_CNS: A Computer Program for the Simulation of Transient, Compressible Flows," Univ. of Queensland Dept. of Mechanical Engineering, Rept. 7/98, 1998.

[24] Wada, Y., and Liou, M. S., "An Accurate and Robust Flux Splitting Scheme for Shock and Contact Discontinuities," *Journal of Scientific Computing*, Vol. 18, No. 3, 1997, pp. 633–657. doi:10.1137/S1064827595287626

[25] Baum, E., King, H. H., and Denison, M. R., "Recent Studies of the Laminar Base-Flow Region," *AIAA Journal*, Vol. 2, No. 9, 1964, pp. 1527–1534. doi:10.2514/3.55084

[26] Chapman, D. R., "Laminar Mixing of a Compressible Fluid," NACA TN 1800, 1950.

[27] Chapman, D. R., Kuehn, D. M., and Larson, H. K., "Investigation of Separated Flows in Supersonic and Subsonic Streams with Emphasis on the Effect of Transition," NACA TR 1356, 1958.

[28] Dewey, C. F., and Gross, J. F., "Exact Similar Solutions of the Laminar Boundary-Layer Equations," *Advances in Heat Transfer*, Vol. 4, 1967, pp. 317–446.

[29] Srivastava, A. C., and Hazarika, G. C., "Shooting Method for Third Order Simultaneous Ordinary Differential Equations with Application to Magnetohydrodynamic Boundary Layer," *Defence Science Journal*, Vol. 40, No. 3, 1990, pp. 263–274.

[30] Kubota, T., and Dewey, C. F., "Momentum Integral Methods for the Laminar Free Shear Layer," *AIAA Journal*, Vol. 2, No. 4, 1964, pp. 625–629. doi:10.2514/3.2398

[31] Dogra, V. K., Moss, J. N., Wilmoth, R. G., Taylor, J. C., and Hassan, H. A., "Effects of Chemistry on Blunt-Body Wake Structure," *AIAA Journal*, Vol. 33, No. 3, 1995, pp. 463–469. doi:10.2514/3.12426

[32] Grasso, F., and Pettinelli, C., "Analysis of Laminar Near-Wake Hypersonic Flows," *Journal of Spacecraft and Rockets*, Vol. 32, No. 6, 1995, pp. 970–980. doi:10.2514/3.26717

[33] Gorshkov, A. B., and Lunev, V. V., "Laminar Base Flow Downstream of Slender Cones in Hypersonic Flow," *Fluid Dynamics*, Vol. 37, No. 5, 2002, pp. 772–783. doi:10.1023/A:1021380605136

[34] Gnoffo, P. A., "Planetary-Entry Gas Dynamics," *Annual Review of Fluid Mechanics*, Vol. 31, No. 1, 1999, pp. 459–494. doi:10.1146/annurev.fluid.31.1.459

[35] Panov, Y. A., and Shvets, A. I., "Study of Flow Structure Behind a Cone in Supersonic Flow," *Fluid Dynamics*, Vol. 2, No. 2, 1967, pp. 96–97. doi:10.1007/BF01015152

[36] Martellucci, A., Trucco, H., and Agnone, A., "Measurements of the Turbulent Near Wake of a Cone at Mach 6," *AIAA Journal*, Vol. 4, No. 3, 1966, pp. 385–391. doi:10.2514/3.3449

[37] Hruschka, R., O'Byrne, S., and Kleine, H., "Two-Component Doppler-Shift Fluorescence Velocimetry Applied to a Generic Planetary Entry Probe Model," *Experiments in Fluids* [online journal], Dec. 2009, http://www.springerlink.com/content/ljj41p7765k56287 [retrieved 25 Dec. 2009]. doi:10.1007/s00348-009-0794-3

[38] Papamoschou, D., "Evidence of Shocklets in a Counterflow Supersonic Shear Layer," *Physics of Fluids*, Vol. 7, No. 2, 1995, pp. 233–235. doi:10.1063/1.868621

[39] Smith, K. M., and Dutton, J. C., "Investigation of Large-Scale Structures in Supersonic Planar Base Flows," *AIAA Journal*, Vol. 34, No. 6, 1996, pp. 1146–1152. doi:10.2514/3.13205

[40] Moss, J. N., Wilmoth, R. G., and Price, J. M., "DSMC Simulations of Blunt Body Flows For Mars Entries: Mars Pathfinder and Mars Microprobe Capsules," 32nd AIAA Thermophysics Conference, Atlanta, GA, AIAA 97-2508, June 1997.

[41] Holden, M. S., "Establishment Time of a Laminar Separated Flow," *AIAA Journal*, Vol. 9, No. 11, 1971, pp. 2296–2298. doi:10.2514/3.6512

[42] Park, G., Hruschka, R., Gai, S. L., and Neely, A. J., "Flow Establishment Behind Blunt Bodies at Hypersonic Speeds in a Shock Tunnel," *Proceedings of SPIE: The International Society for Optical Engineering*, Vol. 7126, 2008, Paper 71260I. doi:10.1117/12.822751

[43] Lees, L., "Laminar Heat Transfer Over Blunt-Nosed Bodies at Hypersonic Flight Speeds," *Jet Propulsion*, Vol. 26, No. 4, 1956, pp. 259–269.

[44] Fay, J. A., and Riddell, F. R., "Theory of Stagnation Point Heat Transfer in Dissociated Air," *Journal of the Aeronautical Sciences*, Vol. 25, Feb. 1958, pp. 73–85.

[45] Gupta, R. N., Lee, K. P., Thompson, R. A., and Yos, J. M., "Calculations and Curve Fits of Thermodynamic and Transport Properties for Equilibrium Air to 30,000 K," NASA Rept. 1260, 1991.

[46] Freeman, G. N., and Oliver, C. C., "High-Temperature Thermodynamic and Transport Properties of Planetary CO_2-N_2 Atmospheres," *AIAA Journal*, Vol. 8, No. 9, 1970, pp. 1687–1693. doi:10.2514/3.5965

[47] Dewey, C. F., "Near-Wake of a Blunt Body at Hypersonic Speeds," *AIAA Journal*, Vol. 3, No. 6, 1965, pp. 1001–1010. doi:10.2514/3.3045

N. Chokani
Associate Editor